# ID 85

# Cementitious Paste Defects Correlated to Engineering Properties of Concrete

Achintyamugdha Sharma[1], Todd Sirotiak[2], Xuhao Wang[3], Peter Taylor[4], Priyanka Deka[5], Ravi Kiran[6] Dayakar Naik[7]

[1] JCMS, Inc., Mercerville, NJ 08619, USA
[2] North Dakota State University, Fargo, ND 58105, USA
[3] Chang'an University, Xi'an, China
[4] Iowa State University, IA 50010, USA
[5] JCMS, Inc., Mercerville, NJ 08619, USA
[6] North Dakota State University, Fargo, ND 58105, USA
[6] University of North Dakota, Grand Forks, ND 58202, USA
asharma@jcms.com

## Abstract

This study was aimed at investigating potential correlations between microstructure properties of cementitious paste samples and bulk properties of hardened concrete. In this study, defects in paste samples were detected and quantified by using X-Ray Micro-Computed Tomography (μ-CT) technique. These quantified defects in paste samples were correlated with bulk properties of corresponding concrete - electrical resistivity, drying shrinkage and degree of hydration from eight cementitious combinations. The results showed correlations between the degree of hydration in concrete and defects in paste. Additionally, the degree of cracking of paste samples can help predict drying shrinkage of resultant concrete.

## Keywords

Cement paste, microstructures, X-Ray Micro CT.

## 1. Introduction

The microstructure of cementitious paste and concrete composites has been extensively investigated by several researchers in the past decades (Jan Bisschop & J. G. M. Van Mier, 2002; J. Bisschop & J. G. M. Van Mier, 2002; Bisschop & van Mier, 2008; de Sa et al., 2008; Golewski, 2018; Monteiro, 2006; Sharma et al., 2020; Shi et al., 2011). In concrete, portland cement acts as the glue to hold coarse aggregates and sand together through hydration reactions that result in the formation of crystals like calcium silicate hydrates (CSH) and calcium hydroxide (CH). The characterization of paste microstructure can reveal the extent of formation of such crystals which in turn can provide useful information about hydration. The rate of hydration depends upon physical and chemical characteristics of cementitious materials used in concrete. Portland cement and pozzolans such as fly ash and nanosilica are carefully chosen by engineers to optimize the production of hydration crystals to refine the microstructure of paste.

Cement paste is the most vulnerable component in concrete to micro-cracks and defects caused by tensile forces due to differential evaporation and volume changes (Bentz, 2006; de Sa et al., 2008). These defects lead to disintegration at the paste-aggregate interface, also known interfacial transition zone (ITZ). As a result, larger cracks are formed in concrete. Deleterious ions like chloride and sulfate can ingress through such cracks. A permeable system of interconnected voids can facilitate the movement of such ions dissolved in pore fluids. After reacting with hydration products, these ions lead to the production of expansive compounds like calcium oxychloride (in case of chloride), and thaumasite and ettringite (in case of sulfate) (Ikumi et al., 2016; Peterson et al., 2013; Whittaker & Black, 2015). As a result, the durability of concrete is compromised. Therefore, characterization of defects and voids in cementitious paste can help in the investigation of durability of concrete.

A material used to impart ductility to concrete composites is fiber. The addition of synthetic or natural fibers can help dissipate tensile energies by transferring load through the fiber-matrix interfacial bond (Abbas & Khan, 2016). Randomly dispersed microfibers with

**Figure 1:** Combined particle size distribution curve for coarse and fine aggregates as per ASTM C33 (ASTM 2018)

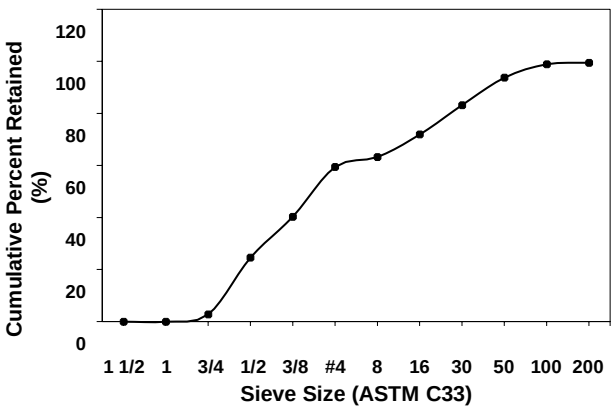


monofilaments having diameter in the micrometer range can be used to provide resistance to microcracking in cementitious paste and concrete (Branston et al., 2016; Yousefieh et al., 2017). A relatively recent and more environment friendly fiber with good mechanical properties is chopped basalt fibers (Katkhuda & Shatarat, 2017). It has reportedly better density, tensile strength and elastic modulus compared to glass fibers (Fiore et al., 2015).

In this study, eight different cementitious combinations comprising of three types of cement (coarse ground, Type I Portland cement, Type IL Portland Limestone Cement), fly ash and nanosilica, and basalt microfibers were investigated. The microstructure of paste samples from these mixtures was investigated to derive indications about the durability of their corresponding concrete samples.

## 2. Materials and Methods

In this study, the microstructure of cementitious paste samples was investigated by using non-destructive technique X-Ray Micro-Computed Tomography (μ-CT). Degree of hydration, electrical resistivity and drying shrinkage of corresponding concrete samples were investigated for comparison.

### 2.1 Materials

In this study, three cement types were used: Coarse Ground portland cement (CG), Type I portland cement (TI), and Type IL portland limestone cement (TIL). Additionally, Class F fly ash (FF), Class C fly ash (FC) and colloidal nanosilica were used as supplementary cementitious materials (SCM). The chemical and physical properties of the cementitious materials are presented in Tables A1 and A2 in Appendix. Chopped basalt fibers 13μm in diameter, and 24 mm in length, treated with a silane-based coating (0.25% w/w) were used per manufacturers recommendations. The dimensions and dosage rate of basalt fibers was also selected as per recommendations from previous literature for optimum performance (Elshafie & Whittleston, 2015). The silane-based coating is provided to protect the fibers in an alkaline environment. In case of concrete samples, ½" (nominal aggregate size) limestone aggregates and locally available sand were used. Figure 1 shows the combined gradation of the aggregates. The water-to-cementitious materials ratio, binder content, and binder to coarse aggregates to fine aggregates weight ratio were fixed at 0.42, 344 kg/m$^3$, and 1:3.08:2.23, respectively. An organic acid-based air entraining agent, and a polycarboxylate based Type F high range water reducing agent (WRA) were used. For paste samples, the water-to-cementitious materials ratio was fixed at 0.40. Paste samples were cast at a lower water-to-cementitious materials ratio in order to minimize bleeding.

### 2.2 Concrete Specimens and Tests

In this study, eight cementitious combinations were investigated: Coarse Ground portland cement (CG-P), Type I ordinary portland cement (TI-P), Type I ordinary portland cement, 30% of which is replaced with Class C fly ash (TI-FC), Type I ordinary portland cement, 20% of which is replaced with Class C fly ash (TI-FF), Type IL Portland Limestone Cement (TIL-P), Type IL Portland Limestone Cement, 30% of which is replaced with Class C fly ash (TIL-FC), Type IL Portland Limestone Cement, 30% of which is replaced with Class C fly ash and 0.25% (v/v) basalt fibers (TIL-FC (B)), and Type I ordinary portland cement, 5% of which is replaced by colloidal nanosilica (TI-NS). The mixture proportions of the concrete used are shown in Table 1. Standard 100 mm x 200 mm cylinders were cast for measuring electrical resistivity (ASTM C1760) and degree of hydration through semi-adiabatic calorimetry (ASTM C1753) (ASTM, 2012, 2015). Shrinkage in the concrete mixtures under restrained conditions was also measured by the standard ring test method specified in ASTM C1581 (ASTM, 2009).

**Table 1:** Mix proportions

| Mix Code | Cement ($kg/m^3$) | Class F Fly Ash ($kg/m^3$) | Class C Fly Ash ($kg/m^3$) | Nano Silica ($kg/m^3$) | ed Basalt Fiber Addition (% v/v) | Water ($kg/m^3$) | WR ($ml/m^3$) | AEA ($ml/m^3$) | Fine Aggregates ($kg/m^3$) | Light Weight Aggregates ($kg/m^3$) | Coarse Aggregates ($kg/m^3$) |
|---|---|---|---|---|---|---|---|---|---|---|---|
| CG-P | 344 | 0 | 0 | 0 | - | 145 | 888 | 45 | 1061 | 0 | 768 |
| TI-P | 344 | 0 | 0 | 0 | - | 145 | 721 | 45 | 1061 | 0 | 768 |
| TI-FC | 241 | 0 | 103 | 0 | - | 145 | 862 | 45 | 1061 | 0 | 768 |
| TI-FF | 275 | 69 | 0 | 0 | - | 145 | 448 | 45 | 1061 | 0 | 768 |
| TIL-P | 344 | 0 | 0 | 0 | - | 145 | 1457 | 45 | 1061 | 0 | 768 |
| TIL-FC | 241 | 0 | 103 | 0 | - | 145 | 971 | 45 | 1061 | 0 | 768 |
| TIL-FC (B) | 241 | 0 | 103 | 0 | 0.25 | 145 | 971 | 45 | 1061 | 0 | 768 |
| TI-NS | 327 | 0 | 0 | 17 | - | 145 | 4280 | 45 | 1061 | 0 | 768 |

## 2.3 Paste Specimens

Cement paste samples were cast for the eight cementitious combinations mentioned in section 2.1.2. For microstructure studies, paste samples were cast in hour-glass shaped 3D printed molds with internal dimensions 0.5”x0.5”x2” (Figure A1). The mold was fabricated using a resin-based 3D printer called Form 2. A 3D CAD model was drafted using Autodesk Fusion 360. The shape of these molds was selected so that stress due to drying shrinkage is maximum along the middle section of the specimens. This would increase the probability of encountering microcracks in this central, thus facilitating the process of imaging. The 3D molds were covered with two plates on the top and bottom, which were fastened using pan-head machine screws (USS #4-40 x ½ in.) the threads were generated using the software. Cement paste was prepared in accordance with ASTM C305 and poured into the molds (ASTM, 2014). All the pieces were also tied together by using rubber bands to provide better water tightness. These samples were then rotated at 10 rotations per minute (Figure A2) for approximately 12 hours to avoid bleeding. Then the samples were wet cured for up to seven days. At the end of seven days from mixing, the top and bottom plates were demolded, and the paste samples allowed to dry under conditions compliant with ASTM C1581 for 28 days (ASTM, 2009).

## 2.4 Micro Computed Tomography

Dried paste samples inside their molds were subjected to X-ray µ-CT scans with a General Electric V|Tome|x s 240, at the NDSU Electron Microscopy Center Core facility. Scanning was done using the 180 kV x-ray tube running at 110 kV, 350 µA, exposure of 333 ms and 1200 images collected per sample. Reconstructed volumes were analyzed with the commercial software package Volume Graphics Studio Max version 3.0. Initially, the Surface Determination mode of the software was used to distinguish between material and background (voids or pores in this case). The surface fit function was applied using the threshold value as the central value between the peaks of material and background in the data histogram. Additionally, an iterative surface determination mode was applied for enhanced precision. This default histogram generated by the software can be used to have an approximate idea of defects within the system. Although the surface determination histogram can be manually fit for detailed detection and quantification of voids as small as 30 µ, for a quick comparison of porosity for voids of size 75 µ and larger, among different cementitious combinations the default method is deemed adequate (Du Plessis et al., 2016). Surface determination was followed by measurement of void sizes by the default Porosity/Inclusions/Defects determination mode of VG Studio Max 3.2. Minimum voxel size was maintained at 8 voxels, and minimum probability of voids was maintained at 0. Figure A3a and A3b show typical examples of 3D reconstruction of paste samples and pores/defects as observed through µ-CT.

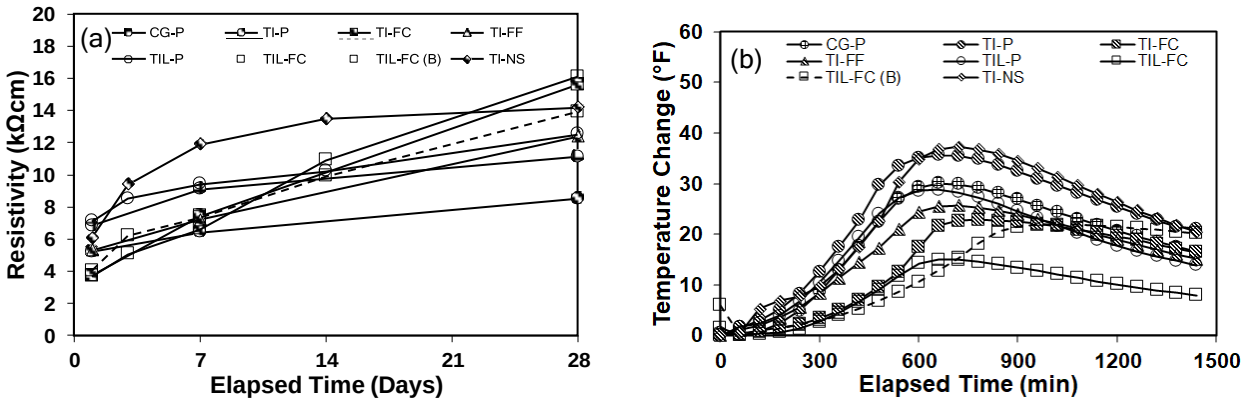


**Figure 2**: (a) Electrical resistivity of concrete, (b) Rate of hydration as measured through semi-adiabatic calorimetry

## 3. Results and Discussions

### 3.1 Paste Microstructure (µ-CT) and Concrete Durability

Figure 2a shows the electrical resistivity results of samples from the concrete mixtures over time elapsed. It is an indirect determination of the durability of the concrete mixtures. The durability of concrete is determined by the ability of the microstructure to resist the passage of deleterious ions like chloride and sulfate through pore fluid. Pore fluid is a better conductor of electricity as compared to cementitious products and aggregates. Therefore, to ensure high durability in concrete an interconnected system of voids capable of transporting pore fluids with dissolved ions should be avoided (Mohr et al., 2000). CG-P is observed to have one of the lowest resistivity results among the eight mixtures. On the other hand, TI-NS appears to have the highest resistivity results through 14 days from mixing. Due to lower fineness of coarse ground cement and a consequently lower surface area compared to other cement types used in this study, the availability of hydration sites should be lower (Bentz, 2010). As a result, the rate of hydration should be slower and consequently, the microstructure of the cementitious system is not as refined when compared to faster reactive systems, like TI-NS, as demonstrated by the peak of temperature change plot obtained through semi-adiabatic calorimetry test (Figure 2b). Due to the presence of nanosilica, the pozzolanic hydration of calcium hydroxide (CH), a by-product of primary hydration reaction, to calcium silicate hydrate (CSH) is driven at a high rate. As a result, a refined microstructure is produced. Nanosilica particles also physically fill interfacial transition zone (ITZ) between cement paste and aggregates (Khaloo et al., 2016; Singh et al., 2013).

Figure 3a and 3b show total defects and average paste diameter of the eight mixtures, respectively. When considering the paste samples of this study, the defects detected and measured through µ-CT could be a combination of voids and cracks. Based on the settings of µ-CT used in this study, the voids detected are roughly more than 100 µm in diameter (assuming the voids to be spherical in shape). Voids of such a size range typically form when free water evaporates without causing any significant tensile stresses (Taylor & Wang, 2014). The availability of free water in turn is dependent on the reactivity of cement and pozzolanicity of supplementary cementitious materials (SCMs). Microcracks can form due to a gradient in relative humidity between subsequent layers of paste resulting in tensile stresses (J. Bisschop & J. G. M. Van Mier, 2002; de Sa et al., 2008). This is mainly because outer layers are drier than the inner ones. From Figure 8a, it is evident that the total number of defects (voids + cracks) observed through µ-CT is the lowest for paste samples from CG-P. In contrast, the paste samples for TI-NS have the highest number of defects. The average pore diameter, however, does not appear to be significantly different between the two mixtures (Figure 3b). As resistivity of the concrete for TI-NS is higher than that of CG-P (Figure 2a), it is likely that the former has a discontinuous system of voids compared to the latter. This trend should also be reflected in their corresponding paste samples. Figures 4a-4h show the void size distribution of the mixtures as observed through µ-CT. From Figure 4h, it is evident that the paste samples of TI-NS have voids distribution with a wide range of sizes. This may be indicative of a discontinuous microstructure with hydration products like CSH crystals filling otherwise larger voids through a rapid hydration process. As a result, the movement of pore water and dissolved ions will be impeded, leading to high electrical resistivity. This is however, not reflected in case of CG-P (Figure 4a).

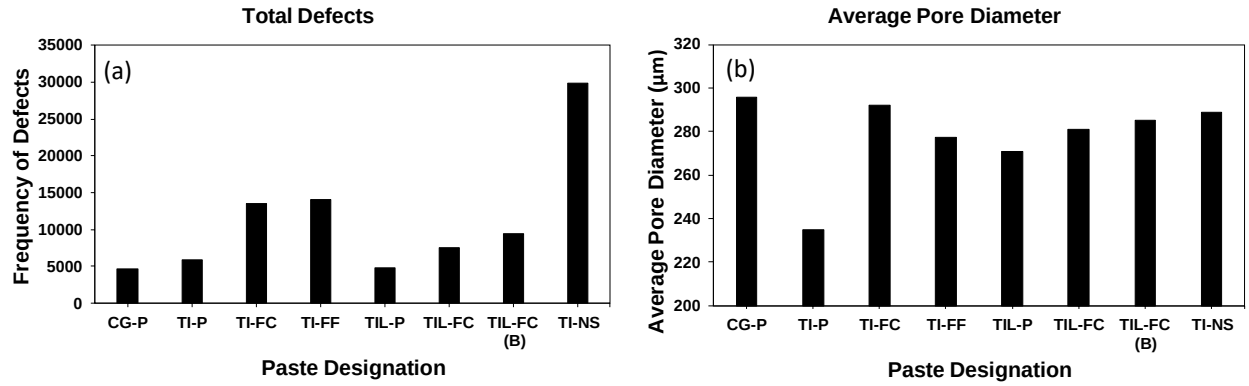


**Figure 3**: µ-CT results for (a) Total defects, (b) Average pore diameter

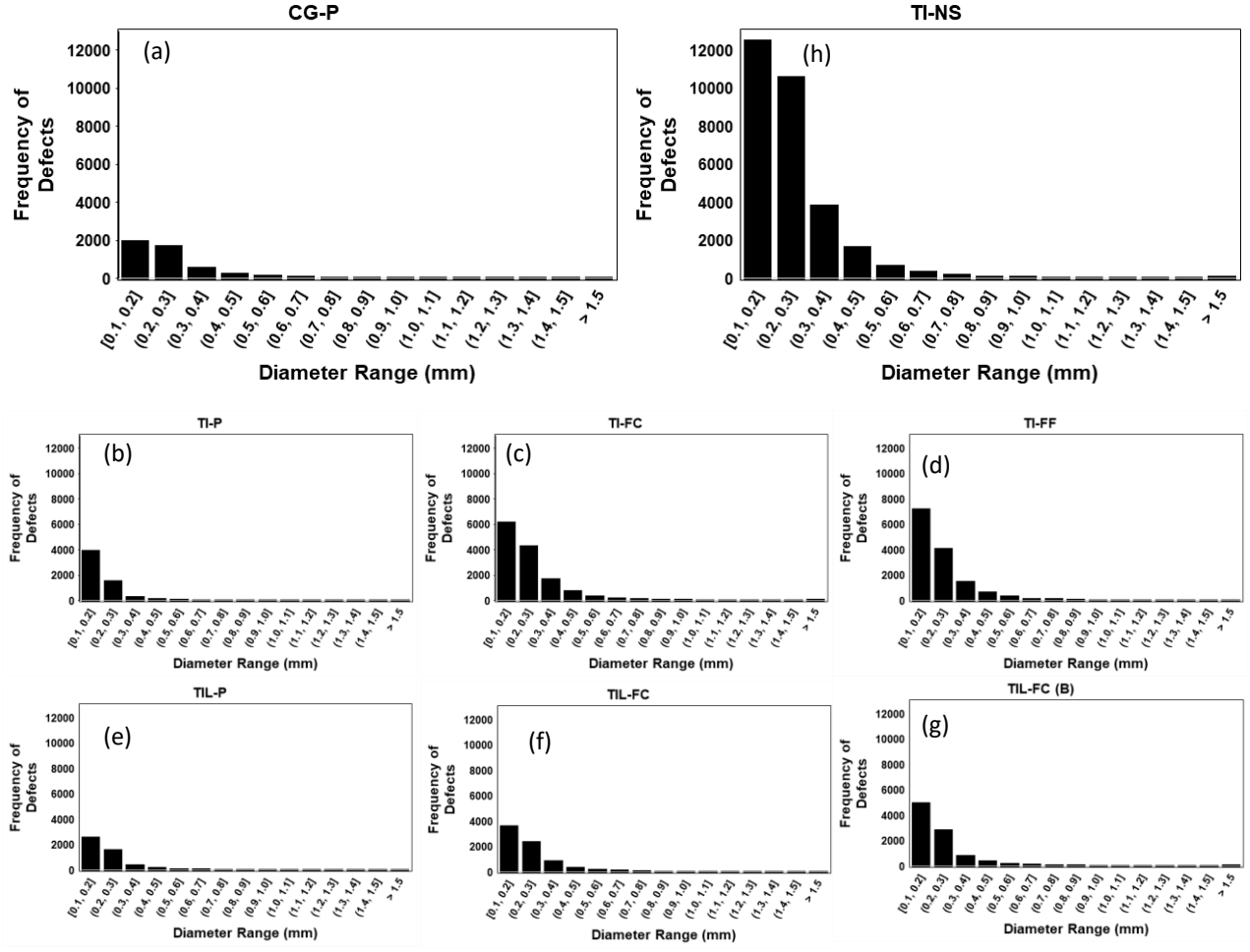


**Figure 4:** Frequency of defects for paste samples of (a) CG-P, (b) TI-P, (c) TI-FC. (d) TI-FF, (e) TIL-P, (f) TIL-FC, (g) TIL-FC (B), (h) TI-NS

The resistivity results of the concrete mixtures containing fly ash (TI-FC, TI-FF, TIL-FC, TIL-FC (B)) are seen to be higher than their control counterparts (TI-P, TIL-P), especially at the later ages (Figure 2a). Mixtures containing fly ash usually have a slower rate of hydration initially (Figure 2b). Fly ash being a pozzolan, helps in refining the microstructure of concrete over time, thereby increasing durability (Celik et al., 2015). Paste samples of TI-FC (Figure 4c), TI-FF (Figure 4d), TIL-FC (Figure 4f) and TIL-FC (B) (Figure 4g) are also seen to have higher frequency of defects and a wider range of void size distribution compared to TI-P (Figure 4b) and TIL-P (Figure 4e). This likely means that due to a refined microstructure created by fly ash, the likelihood of a continuous system of voids is reduced (Chindaprasirt et al., 2004; De Weerdt et al., 2011).

### 3.2 Paste Defects and Degree of Hydration of Concrete

The microstructure of a cement paste is formed by crystals like calcium silicate hydrate (CSH) and calcium hydroxide (CH) which are formed through the process of hydration (Wilson & Kosmatka, 2011). The rate of these hydration reactions determines the rate of formation of such crystals which in turn determines how refined the hardened paste microstructure is (Cheung et al., 2011). From Figure 5a and 5b, a correlation can be seen between total defects found in paste and the slope of the peak of the rate hydration-time curve as measured through semi-adiabatic calorimetry technique. An example of the method of calculating the slope of the peak of hydration is shown in Figure 5c. The relationship between total defects in paste and peak rate of hydration of concrete appear to manifest differently in case of mixtures with and without supplementary cementitious materials (SCMs) (Figures 5a and 5b). The presence of pozzolans (fly ash and nanosilica in this study) help with additional formation of CSH gel through hydration of CH, a by-product of primary hydration of cement (Wilson & Kosmatka, 2011). These additional crystals likely partially fill voids, thus converting a system of a smaller number of larger voids/defects into that of larger number of relatively smaller voids/defects (Figure A4) (Golewski, 2018). As the dissolution of cement minerals like alite (tricalcium silicate) is anisotropic, the orientation and nucleation of CSH crystals in three dimensions may explain the differences in the number of defects vs. slope of peak rate of hydration curves in case of mixtures with and without SCMs (Figures 10a, 10b) (Robin et al., 2018).

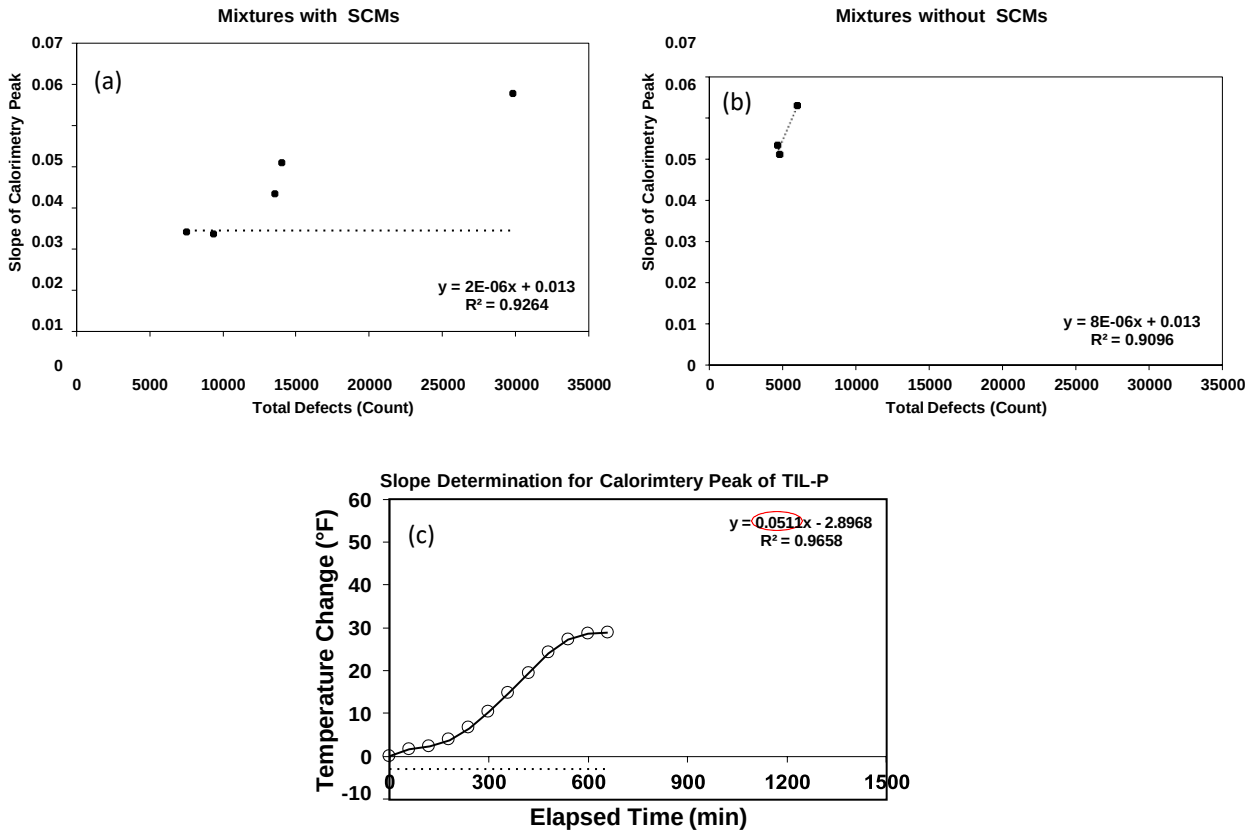


**Figure 5**: Total defects in paste vs. slope of peak of calorimetry curve of concrete for (a) mixtures without SCMs, (b) mixtures with SCMs, (c) slope of peak of calorimetry curve in TIL-P

### 3.3 Paste Microstructure (μ-CT) and Concrete Shrinkage

From Figure 6a, the average stress rate, derived from drying shrinkage strain under restrained conditions, appears to be a function of the total defects in paste as observed through μ-CT. When free water evaporates from paste, it leaves voids behind. When tensile forces are formed due to gradients in relative humidity between subsequent layers of cement paste, such materials may have a tendency to collapse into these voids (Jan Bisschop & J. G. M. Van Mier, 2002; de Sa et al., 2008). Therefore, a higher number of voids in paste may indicate a high shrinkage strain in concrete.

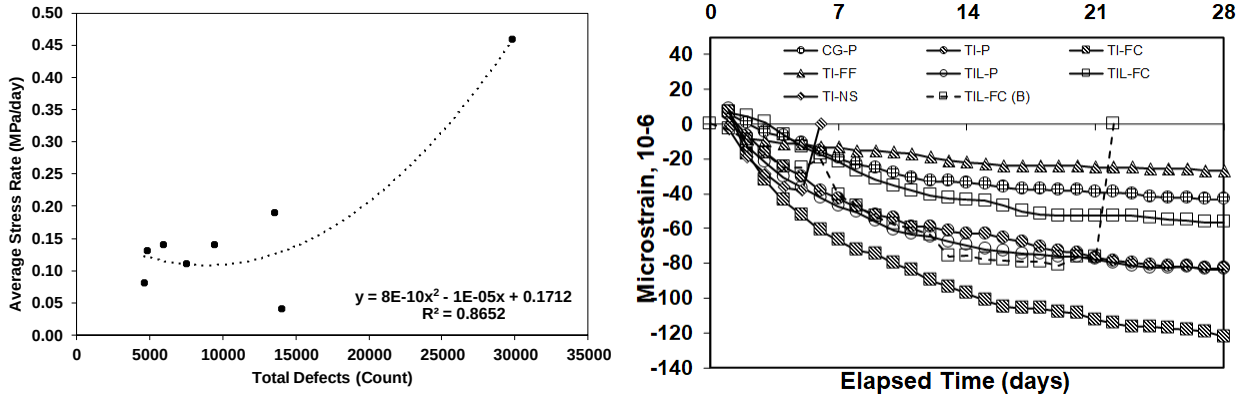


**Figure 6:** (a) Total defects in paste from μ-CT vs. average stress rate from restrained drying shrinkage in concrete, (b) Drying shrinkage strain for concrete mixtures

Figure 6b shows the drying shrinkage strain for the eight mixtures plotted against elapsed time. Among the mixtures with no supplementary cementitious materials (SCMs), CG-P appears to have the lowest shrinkage strain. Prior researchers have also reported lower shrinkage strain for concrete containing coarser cementitious systems (Deshpande, 2007; Mehta & Burrows, 2001; Sharma et al., 2019; Tritsch et al., 2005). TI-FC is seen to have higher shrinkage strain than TI-P. This is consistent with prior literature (Munday et al.). Higher drying shrinkage strain was reported by prior researchers in case of concrete containing fly ash with an unaltered water/binder ratio as compared to control (Nath & Sarker, 2013). This is likely because of a higher availability of free water in case of mixtures containing fly ash as it can help maintain workability with lower amounts of water due to the presence of spherical glassy particles (Jiang & Malhotra, 2000). The curves for TI-NS and TIL-FC (B) appear to abruptly drop to zero indicating cracks in the concrete ring (ASTM C1581).

## Conclusions

Based on the findings of this study, it is seen that the electrical resistivity results for TI-NS is the highest among all mixtures, while that for CG-P appears to be the lowest. The degree of hydration (as observed through temperature change plot over elapsed time from semi-adiabatic calorimetry test) appears to influence electrical resistivity results of the mixtures. Total defects (voids + cracks) observed through μ-CT is the lowest for CG-P and highest for TI-NS. Additionally, TI-NS shows voids of a wide range of sizes likely indicating a growth of hydration products like CSH to develop a discontinuous microstructure. The mixtures containing fly ash have higher electrical resistivity results compared to their control counterparts. Moreover, the paste samples containing fly ash have higher number of total defects with void sizes distributed on a wide range of sizes likely indicating a discontinuous microstructure. In this study, total defects in paste appear to have a correlation with degree of hydration of concrete. The relationship between degree of hydration of concrete and total defects in paste shows different trends in case of mixtures with and without SCMs, likely due to anisotropic dissolution of cement minerals. Finally, drying shrinkage of concrete appears to be related to quantification of defects in paste.

## References


Abbas, M. Y., & Khan, M. I. (2016). Fiber-Matrix Interfacial Behavior of Hooked-End Steel Fiber-Reinforced Concrete. *Journal of Materials in Civil Engineering*, *28*(11), 04016115.

ASTM. (2009). Standard Test Method for Determining Age at Cracking and Induced Tensile

Stress Characteristics of Mortar and Concrete under Restrained Shrinkage. In *C1581/C1581M-09a*. West Conshohocken, PA.

ASTM. (2012). Standard Test Method for Bulk Electrical Conductivity of Hardened

Concrete. In *C1760-12*. West Conshohocken, PA.
ASTM. (2014). Standard Practice for Mechanical Mixing of Hydraulic Cement Pastes and Mortars of Plastic Consistency. In *C305*. West Conshohocken, PA.
ASTM. (2015). Standard Practice for Evaluating Early Hydration of Hydraulic

Cementitious Mixtures Using Thermal Measurements. In *C1753/C1753M-15e1*. West Conshohocken, PA.
Bentz, D. P. (2006). Influence of Shrinkage-Reducing Admixtures on Early-Age Properties of Cement Pastes. *Journal of Advanced Concrete Technology*, *4*(3), 423-429. https://doi.org/10.3151/jact.4.423
Bentz, D. P. (2010). Blending different fineness cements to engineer the properties of cement-based materials. *Magazine of Concrete Research*, *62*(5), 327-338.
Bisschop, J., & Van Mier, J. G. M. (2002). Drying shrinkage microcracking in cement-based materials. *Heron, 47 (3), 2002*.
Bisschop, J., & Van Mier, J. G. M. (2002). How to study drying shrinkage microcracking in cement-based materials using optical and scanning electron microscopy? *Cement and concrete research*, *32*(2), 279-287.
Bisschop, J., & van Mier, J. G. M. (2008). Effect of aggregates and microcracks on the drying rate of cementitious composites. *Cement and Concrete Research*, *38*(10), 1190-1196.
Branston, J., Das, S., Kenno, S. Y., & Taylor, C. (2016). Influence of basalt fibres on free and restrained plastic shrinkage. *Cement and Concrete Composites*, *74*, 182-190.
Celik, K., Meral, C., Gursel, A. P., Mehta, P. K., Horvath, A., & Monteiro, P. J. M. (2015). Mechanical properties, durability, and life-cycle assessment of self-consolidating concrete mixtures made with blended portland cements containing fly ash and limestone powder. *Cement and Concrete Composites*, *56*, 59-72.
Cheung, J., Jeknavorian, A., Roberts, L., & Silva, D. (2011). Impact of admixtures on the hydration kinetics of Portland cement. *Cement and concrete research*, *41*(12), 1289-1309.
Chindaprasirt, P., Homwuttiwong, S., & Sirivivatnanon, V. (2004). Influence of fly ash fineness on strength, drying shrinkage and sulfate resistance of blended cement mortar. *Cement and Concrete Research*, *34*(7), 1087-1092.
de Sa, C., Benboudjema, F., Thiery, M., & Sicard, J. (2008). Analysis of microcracking induced by differential drying shrinkage. *Cement and Concrete Composites*, *30*(10), 947-956.
De Weerdt, K., Haha, M. B., Le Saout, G., Kjellsen, K. O., Justnes, H., & Lothenbach, B. (2011). Hydration mechanisms of ternary Portland cements containing limestone powder and fly ash. *Cement and Concrete Research*, *41*(3), 279-291.
Deshpande, S. S. (2007). *Evaluating free shrinkage of concrete for control of cracking in bridge decks*. University of Kansas.
Du Plessis, A., Olawuyi, B. J., Boshoff, W. P., & Le Roux, S. G. (2016). Simple and fast porosity analysis of concrete using X-ray computed tomography. *Materials and Structures*, *49*(1-2), 553-562.
Elshafie, S., & Whittleston, G. (2015). A review of the effect of basalt fibre lengths and proportions on the mechanical properties of concrete. *International Journal of Research in Engineering and Technology*, *4*(01), 458-465.
Fiore, V., Scalici, T., Di Bella, G., & Valenza, A. (2015). A review on basalt fibre and its composites. *Composites Part B: Engineering*, *74*, 74-94.
Golewski, G. L. (2018). Evaluation of morphology and size of cracks of the Interfacial Transition Zone (ITZ) in concrete containing fly ash (FA). *Journal of hazardous materials*, *357*, 298-304.
Ikumi, T., Cavalaro, S. H. P., Segura, I., de la Fuente, A., & Aguado, A. (2016). Simplified methodology to evaluate the external sulfate attack in concrete structures. *Materials & Design*, *89*, 1147-1160.
Jiang, L. H., & Malhotra, V. M. (2000). Reduction in water demand of non-air-entrained concrete incorporating large volumes of fly ash. *Cement and Concrete Research*, *30*(11), 1785-1789.
Katkhuda, H., & Shatarat, N. (2017). Improving the mechanical properties of recycled concrete aggregate using chopped basalt fibers and acid treatment. *Construction and Building Materials*, *140*, 328-335.
Khaloo, A., Mobini, M. H., & Hosseini, P. (2016). Influence of different types of nano-SiO 2 particles on properties of high-performance concrete. *Construction and Building Materials*, *113*, 188-201.
Mehta, P. K., & Burrows, R. W. (2001). Building durable structures in the 21 st century. *Indian Concrete Journal*, *75*(7), 437-443.
Mohr, P., Hansen, W., Jensen, E., & Pane, I. (2000). *Transport properties of concrete pavements with excellent long-term in-service performance* (Vol. 30). https://doi.org/10.1016/s0008-8846(00)00452-x
Monteiro, P. (2006). *Concrete: microstructure, properties, and materials*. McGraw-Hill Publishing.

Munday, J. G. L., Ong, L. T., Wong, L. B., & Dhir, R. K. (1982). Load independent movements in opc/pfa concrete.
Nath, P., & Sarker, P. K. (2013). Effect of mixture proportions on the drying shrinkage and permeation properties of high strength concrete containing class F fly ash. *KSCE Journal of Civil Engineering*, *17*(6), 1437-1445.
Peterson, K., Julio-Betancourt, G., Sutter, L., Hooton, R. D., & Johnston, D. (2013). Observations of chloride ingress and calcium oxychloride formation in laboratory concrete and mortar at 5 C. *Cement and Concrete Research*, *45*, 79-90.
Robin, V., Wild, B., Daval, D., Pollet-Villard, M., Nonat, A., & Nicoleau, L. (2018). Experimental study and numerical simulation of the dissolution anisotropy of tricalcium silicate. *Chemical Geology*, *497*, 64-73.
Sharma, A., Angadi, P., Sirotiak, T., Wang, X., Taylor, P., Borowicz, P., & Payne, S. (2020). Characterization of paste microstructure for durability properties of concrete. *Construction and Building Materials*, *248*, 118570.
Sharma, A., Sirotiak, T., Wang, X., Taylor, P., Angadi, P., & Payne, S. (2019). Portland limestone cement for reduced shrinkage and enhanced durability of concrete. *Magazine of Concrete Research*, 1-16.
Shi, X., Fay, L., Peterson, M. M., Berry, M., & Mooney, M. (2011). A FESEM/EDX investigation into how continuous deicer exposure affects the chemistry of Portland cement concrete. *Construction and building materials*, *25*(2), 957-966.
Singh, L. P., Karade, S. R., Bhattacharyya, S. K., Yousuf, M. M., & Ahalawat, S. (2013). Beneficial role of nanosilica in cement based materials–A review. *Construction and Building Materials*, *47*, 1069-1077.
Taylor, P., & Wang, X. (2014). Concrete Pavement Mixture Design and Analysis (MDA): Factors Influencing Drying Shrinkage.
Tritsch, N., Darwin, D., & Browning, J. (2005). *Evaluating Shrinkage and Cracking Behavior of Concrete Using Restrained Ring and Free Shrinkage Tests.*
Whittaker, M., & Black, L. (2015). Current knowledge of external sulfate attack. *Advances in Cement Research*.
Wilson, M. L., & Kosmatka, S. H. (2011). Design and Control of Concrete Mixtures. Portland Cement Association. In: Skokie.
Yousefieh, N., Joshaghani, A., Hajibandeh, E., & Shekarchi, M. (2017). Influence of fibers on drying shrinkage in restrained concrete. *Construction and Building Materials*, *148*, 833-845.

## Appendix

Table A1: Chemical and physical properties of cements used

| **Item** | **Coarse Ground Cement*** | **Type I Cement*** | **Type IL Cement**** | **Class C Fly Ash***** | **Class F Fly Ash***** |
|---|---|---|---|---|---|
| $SiO_2$ (%) | 21.07 | 19.80 | - | 39.01 | 51.65 |
| $Al_2O_3$ (%) | 4.25 | 4.90 | - | 21.23 | 16.29 |
| $Fe_2O_3$ (%) | 3.13 | 2.40 | - | 5.72 | 5.63 |
| CaO (%) | 65.00 | 63.40 | - | 24.31 | 13.00 |
| MgO (%) | 0.97 | 2.80 | 0.90 | 5.31 | 4.26 |
| $SO_3$ (%) | 2.88 | 3.00 | 3.10 | 0.81 | 0.67 |
| $SiO_2+Al_2O_3+Fe_2O_3$ | - | - | - | 65.96 | 73.57 |
| Loss on ignition (%) | 0.75 | 2.60 | 4.80 | 0.16 | 0.10 |
| $Na_2O$ (%) | 0.14 | 0.04 | - | 1.58 | 3.23 |
| $K_2O$ (%) | 0.58 | 0.73 | - | 0.53 | 2.45 |
| Insoluble Residue (%) | 0.21 | 0.34 | 0.40 | | |
| $CO_2$ (%) | - | 1.50 | - | | |
| Limestone (%) | - | 3.7 | 10.0 | | |

| | | | | | |
|---|---|---|---|---|---|
| $CaCO_3$ in limestone (%) | - | 93.00 | 96.20 | | |
| $C_3S$ (%) | 61.62 | 60.00 | - | | |
| $C_2S$ (%) | 12.44 | 9.00 | - | | |
| $C_3A$ (%) | 5.83 | 9.00 | 7.00 | | |
| $C_4AF$ (%) | 9.3 | 7.00 | - | | |
| Equivalent alkalies (%) | 0.52 | 0.52 | - | 1.15 | 1.63 |
| Blaine Fineness ($m^2/kg$)**** | 316.94 | 397.00 | 382.00 | | |
| Fineness (+325 Mesh) (%)**** | - | - | - | 16.90 | 21.29 |

*Limits specified in ASTM C150
**Limits specified in ASTM C595
***Limits specified in ASTM C618
****Physical property

Table A2: Chemical and physical properties of nanosilica used

| **Item** | **Colloidal Nanosilica** |
|---|---|
| $SiO_2$ (%) | 49.0-51.0 |
| $SiO_2$:$Na_2O$ Ratio | 200-250 |
| $Na_2SO_4$ (%) | ≤0.135 |
| pH | 8.5-9.5 |
| Viscosity (at 25°C) (cps)* | ≤55 |
| Specific Gravity (at 60°F)* | 1.388-1.407 |
| Surface Area ($m^2/g$)* | 110-150 |

*Physical properties

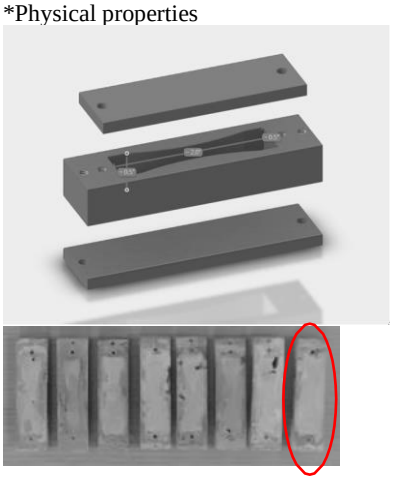

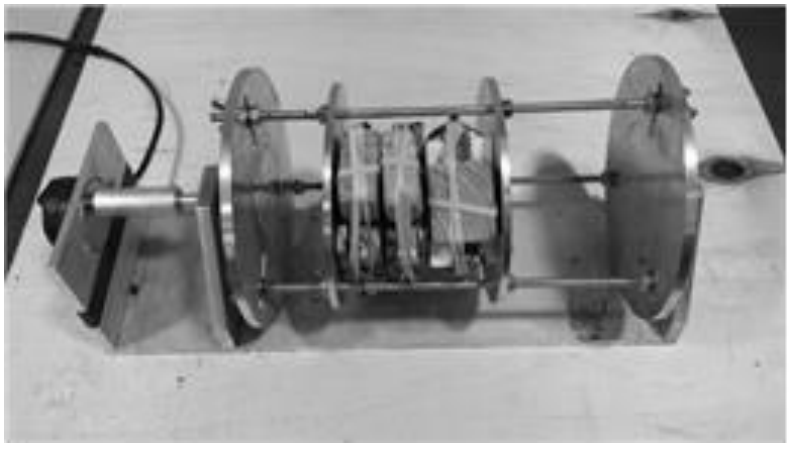

**Figure A1**: 3D Printed Resin Based Mold for Paste Sample, A2: End-to-end rotating device setup for paste samples

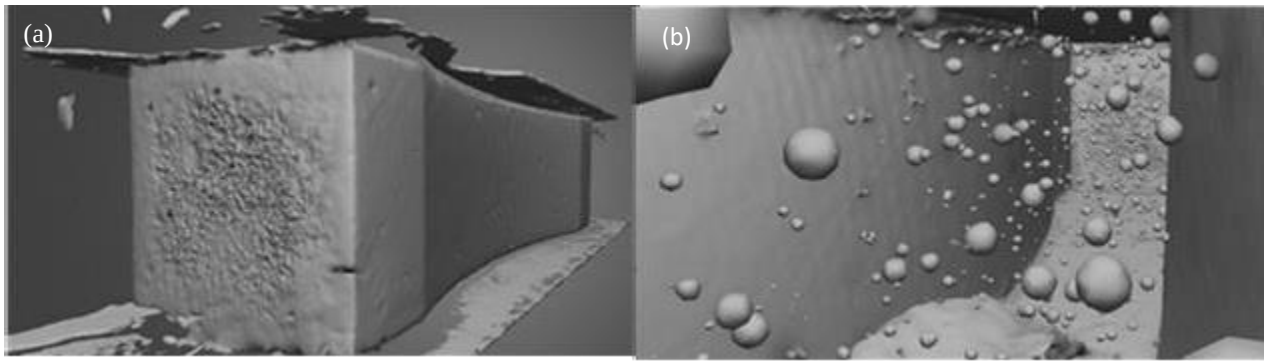


**Figure A3:** µ-CT Results for (a) 3D reconstruction of a paste sample (b) 3D reconstruction of pore distribution inside a paste sample

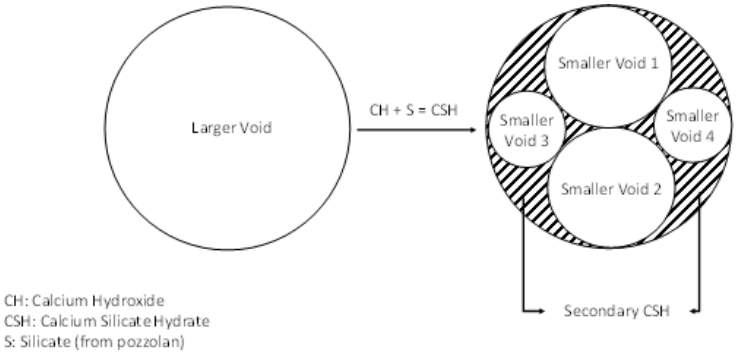


**Figure A4:** Conversion of larger voids into multiple smaller voids by pozzolan